

## Melting of basaltic lithologies in the Earth's lower mantle



Marzena A. Baron<sup>a,2,\*</sup>, Guillaume Fiquet<sup>a</sup>, Guillaume Morard<sup>a,b</sup>, Francesca Miozzi<sup>a,1</sup>, Imène Esteve<sup>a</sup>, Béatrice Doisneau<sup>a</sup>, Anna S. Pakhomova<sup>c,3</sup>, Yanick Ricard<sup>d</sup>, François Guyot<sup>a</sup>

<sup>a</sup> Sorbonne Université, Institut de Minéralogie, de Physique des Matériaux et de Cosmochimie, Museum National d'Histoire Naturelle, UMR CNRS 7590, Paris, France.

<sup>b</sup> Université Grenoble Alpes, CNRS, ISTerre, Grenoble, France.

<sup>c</sup> Deutsches Elektronen-Synchrotron (DESY), Hamburg, Germany.

<sup>d</sup> Université de Lyon, École normale supérieure de Lyon, UCBL, Laboratoire LGLTPE, Lyon, France.

### ARTICLE INFO

#### Keywords:

Basalt  
Earth's lower mantle  
X-ray diffraction  
Elemental partitioning  
Melting  
Laser heated diamond anvil cell, electron microscopy

### ABSTRACT

As basaltic rocks formed at the base of the oceanic floor are transported back to the Earth's mantle along subduction zones, they undergo transitions and introduce compositional and thermal heterogeneities in the deeper parts of the mantle. Studying the melting phase relations of basaltic lithologies at elevated pressures and temperatures provides insights into what potentially happens at different depths in the lower mantle now and throughout the past billion years of active plate tectonics. Using laser heated – diamond anvil cell experiments combined with *in situ* X-Ray Diffraction measurements at synchrotron sources, we revisit the crystallization and melting properties of natural basaltic samples at 60–100 GPa and up to 4000 K. Diffraction patterns highlight the major phases: bridgmanite and Ca-perovskite, followed by crystallization of Si-rich phases (mainly stishovite) and Calcium Ferrite (*CF*-type) Na and Al-rich phase. Recovered samples were prepared using focused ion beam techniques for detailed chemical analyses of the extracted thin sections by electron microscopies in order to resolve sub-micron features and understand the chemical partitioning of elements induced by melting at high pressure and temperature conditions. We confirm that the liquidus phase is Ca-perovskite, which segregates during melting and is recovered as rings that encapsulate a melt pool throughout the studied pressure range. The melt pocket shows a concentric structure consisting of an alumino-silicate envelope surrounding an Fe-rich silicate part. At the center of samples, an Fe-O-S metal pond is often observed. We associate the observation of segregation of liquid phases to capillary forces. The differentiation of melt pockets into three melts is tentatively attributed to Marangoni effects, *i.e.* temperature-induced surface tension gradients in the samples. Central metal ponds are indirectly best interpreted as related to the disproportionation reaction of  $\text{Fe}^{2+}$  into  $\text{Fe}^{3+}$  and  $\text{Fe}^{(0)}$  in bridgmanite whereas the two silicate-melt pools could be associated to the formation of two immiscible liquids upon melting of basalts. On the basis of these observations, we propose that melting of basaltic lithologies at lower mantle pressures could lead to important chemical differentiation mostly characterized by Fe enrichment at increasing depth.

### 1. Introduction

The fate of basaltic and peridotitic material in the lower mantle has been a topic of experimental and computational research since decades. Linking geological observations of processes happening near and at the Earth's surface (*e.g.* volcanic activity and deep earthquakes related to the movement of the lithospheric plates) with seismic tomography

images (*e.g.* van der Hilst et al., 1997; Fukao and Obayashi, 2013), provides clear evidence of the dynamic nature of the Earth's interior. Furthermore, three-dimensional geodynamic simulations (*e.g.* Tackley et al., 1993; Nakagawa and Tackley, 2008) of the Earth's interior also support the concept of a whole-mantle convection. Thanks to advances in the geophysical observations of large- and small-scale heterogeneities in the Earth's mantle, we have now improved our understanding of the

\* Corresponding author.

E-mail address: [marzena.a.baron@gmail.com](mailto:marzena.a.baron@gmail.com) (M.A. Baron).

<sup>1</sup> Now at: Earth and Planets Laboratory, Carnegie Institution for Science, Washington, DC, USA.

<sup>2</sup> Now at: Sorbonne Université, CNRS, Laboratoire Chimie de la Matière Condensée de Paris (CMCP), Paris, France.

<sup>3</sup> Now at: European Synchrotron Radiation Facility, Grenoble, France.

various plate tectonics setups, including different subduction scenarios and their role in the overall geodynamic cycle. Since the discovery of plate tectonics, it has been suggested that the oceanic plates undergo subduction into the deeper parts of the interior, but only just recently the different stages of this recycling process were captured (e.g. van der Meer et al., 2018). Improved global mantle tomography models led to interpretations of lower-mantle slab structure and at this very moment, we have evidence of younger slabs briefly stagnating at depth between 660 and 1000 km (e.g. Caribbean slab under Lesser Antilles arc) and some older slabs already reaching the core-mantle boundary (e.g. Tonga–Kermadec–Hikurangi slab under Fiji). The present-day global mantle structure has also led to estimates of paleo-subduction zones and how that relates to our planet's dynamic evolution of the past ~300 Myr (e.g. Ricard et al., 1993; Torsvik et al., 2006; van der Meer et al., 2018).

Although the averaged structure of the bulk mantle resembles the mineralogy of peridotite with major phase transitions associated with the seismically resolvable discontinuities at 410 and 660 km depth, a more heterogeneous picture emerges from a detailed study of the geophysical data. The subducted mid-ocean ridge basaltic (MORB) material is different from the ambient lower mantle and therefore introduces chemical and thermal heterogeneities. One of the most distinct features in the lowermost part of the Earth's mantle is the laterally and vertically heterogeneous D'' zone near the CMB (core-mantle boundary, e.g. Garnero and McNamara, 2008; Lay et al., 2008; Torsvik et al., 2010, 2016; Trønnes et al., 2018). The origin, composition and properties of these heterogeneities remain uncertain and are a subject of multidisciplinary discussions. The two antipodal large low shear-wave velocity provinces (LLSVPs) located underneath Africa and the Pacific and more localized ultra-low velocity zones (ULVZs) may be a result of either fractional crystallization of the magma ocean during the earliest history of the Earth and/or the continued accretion of subducted basaltic oceanic crust at the CMB (e.g. Labrosse et al., 2007; McNamara et al., 2010; Elkins-Tanton, 2012; Torsvik et al., 2016) or both. In order to test both hypotheses, a good understanding of the melting phase relations of peridotitic and basaltic compositions are required throughout the whole mantle pressure range.

Melting phase relations of basaltic and peridotitic lithologies have been studied experimentally in multi-anvil presses up to the upper-lower mantle boundary (25 GPa) and laser-heated diamond anvil cell (LH-DAC) melting experiments until core-mantle boundary (135 GPa). The LH-DAC experiments on natural multi-component peridotitic (e.g. Fiquet et al., 2010; Andrault et al., 2011; Nomura et al., 2014) and basaltic compositions (e.g. Hirose et al., 1999; Andrault et al., 2014; Pradhan et al., 2015; Tateno et al., 2018) yield a range of solidus and liquidus temperatures at lower mantle pressures. It has been so far difficult to discriminate between the effects of bulk composition, the presence or absence of volatiles in starting materials, various experimental setups (e.g. pressure medium effect) and the different melting criteria and detection techniques used to establish the melting curves and correctly interpret the chemistry in the run products. It should also be noted that, in the early studies, the chemical characterization of recovered samples has only been partially addressed, mainly focusing on determination of partition coefficients of Fe, Si and Mg, due to difficulties with sample recovery and analytical limitations. More in-depth chemical investigations have been presented by Pradhan et al. (2015) and Tateno et al. (2018), who focused on the small zone between the melt pocket and the liquidus phase instead of the entire sample. Finally, systematic studies of chemically simpler systems were also carried in order to assess the stability and understand the melting behaviour of lower mantle phases and eutectics in the MgO-SiO<sub>2</sub>, MgO-FeO-SiO<sub>2</sub> and CaO-MgO-SiO<sub>2</sub> systems (e.g. Liebske and Frost, 2012; Boukaré et al., 2015; Baron et al., 2017; Nomura et al., 2017; Nabe et al., 2021).

Here, we present the results of our newest experimental and analytical study of melting natural basaltic lithologies at pressures of the Earth's lower mantle. We combined laser-heated diamond anvil cell (LH-DAC) experiments performed at 60–100 GPa and 3000–4000 K,

with *in situ* synchrotron-based X-ray diffraction (XRD) measurements as well as multistep *ex situ* characterization of recovered samples using focused ion beam (FIB) preparation for analyses of chemistry and textures with electron microscopies. Our main goal in the present study is to constrain the issues of crystallization sequence, elemental distribution between melts and crystalline material, by testing various experimental setups and pressure media, and to interpret the complex quenched features of the LH-DAC experiments. This will allow us to finally understand the mechanisms of the recycling of the basaltic lithologies back in the lower mantle. In the end, we will also present potential physical explanation for melt segregation which commonly occurs in the LH-DAC experiments when melting occurs and which has been poorly described so far, possibly resulting in misleading interpretations of melt features and their chemistry.

## 2. Experimental and analytical methods

### 2.1. Starting composition and pressure media

The starting composition used in this study was a natural MORB glass from the East Pacific Rise, where new oceanic crust is being formed. In Table 1 the chemical composition of our starting material is listed together with examples of other basaltic samples, which were used in previously published experiments. Our basaltic material is relatively rich in minor elements like S, Mn, K and Na (see Table 1, (E)) but overall, major elemental concentrations are similar to other standards used in the literature. Glassy pieces homogeneous in compositions were extracted from geological thin sections (10–20 µm thick) and placed in between two discs of previously prepared pressure medium substances (PM). We have used two types of PM: crystalline KCl and amorphous Al<sub>2</sub>O<sub>3</sub>. Dried grains of KCl were cold pressed into sheets out of which disks of selected diameters were pre-cut by a femto-second laser and stored at 125 °C to avoid moisture. The amorphous Al<sub>2</sub>O<sub>3</sub> was deposited using physical vapour deposition methods (see details in Morard, 2017). The discs served not only as pressure transmitting media and thermal insulators but also as reliable pressure calibrants. The PM-sample-PM sandwiches were then loaded in a pre-indented rhodium gasket (initially 200 µm thick) prepared for 'Princeton-type' symmetric DACs, with drilled holes of 80, 55 and 35 µm for diamonds with flat culets of 200 µm and beveled culets of 150/300 and 100/300-µm diameters, respectively. A small ruby sphere was added on the side of the sample chamber, away from the centre of the basaltic sample for pressure measurement during compression. Before pressurising, the loaded but not closed DACs were heated for an hour at 125 °C to remove any absorbed moisture during loading manipulations.

**Table 1**  
Chemical composition of basaltic lithologies used in high-pressure and high-temperature experimental studies.

	BIR-1 standard	(A) + (B)	(C)	(D)	(E) + this study
SiO <sub>2</sub>	47.96	49.64	51	50.73	49.74
TiO <sub>2</sub>	0.96	1.64	1.7	2	1.33
Al <sub>2</sub> O <sub>3</sub>	15.5	14.88	15.7	13.73	15.89
FeO	10.4	11.43	9.9	11.29	9.73
MgO	9.7	8.51	7.7	6.76	8.46
CaO	13.3	10.55	11.2	10.94	11.74
Na <sub>2</sub> O	1.82	2.9	2.4	2.83	2.69
K <sub>2</sub> O	0.03	0.12	0.2	0.15	0.1
P <sub>2</sub> O <sub>5</sub>	0.021				0.11
MnO	0.175	0.18		0.2	0.18
S				0.15	0.14
Cr <sub>2</sub> O <sub>3</sub>					0.04
Total	99.866	99.85	99.8	98.78	100.15

(A) Hirose et al., 1999; (B) Tateno et al., 2018; (C) Ono et al., 2005; (D) Andrault et al., 2014; (E) Pradhan et al., 2015.

## 2.2. LH-DAC experiments with *in-situ* X-ray diffraction measurements

All experiments were performed using the laser-heated diamond anvil cell (LH-DAC) system installed at the P02.2 Extreme Conditions Beamline (ECB) at Petra III in the Deutsche Elektronen Synchrotron (DESY) (Liermann et al., 2015) in order to collect *in situ* X-ray diffraction (XRD) patterns.

At the synchrotron P02.2 beamline, the monochromatic beam of 42.65 KeV ( $\lambda = 0.2907 \text{ \AA}$ ) was focused on a sample area of about  $6 \mu\text{m} \times 4 \mu\text{m}$ . The diffraction signal was collected on a PerkinElmer detector with an exposure time between 5 and 10 s. Laser heating experiments were performed with an on-axis double-sided laser heating setup equipped with a 200 W Yb-fibre laser which was split by a polarizing beam splitter into two Gaussian profile beams (upstream and downstream). Typical laser spot size was  $\sim 10\text{--}20 \mu\text{m}$  in diameter. The emitted light from the laser-heated sample was then collected from both sides by a system of mirrors and lenses and guided to the spectrograph entrance slit and CCD camera (Andor technology). The transfer function of the optical system for temperature measurement was calibrated using a tungsten halogen lamp at 2200, 2500 and 2900 K. Spectra from hot samples were used for temperature estimation by fitting procedure to the Planck's law using the software T-Rax by C. Prescher. The error on the temperature measurement was on the order of  $\pm 150 \text{ K}$ , which results from the measurement uncertainties, including temperature gradients, heating instability, and accuracy of the grey body approximation.

Sample to detector distance and detector orientation were calibrated with a cerium dioxide ( $\text{CeO}_2$ ) standard. Collected diffraction images were radially integrated using the software Dioptras (Prescher and Prakapenka, 2015) and analysed with the diffraction software PDIndexer

(Seto et al., 2010).

The cells were pressurised to the target pressures at room temperature before laser-heating, using the R1 ruby fluorescence peak shift measurements (Mao et al., 1986). During each experiment, pressure was directly measured from the XRD pattern of the pressure transmitting media. The reported pressures in this study are always the post-heating measurements based on the quenched XRD patterns of KCl (Deweale et al., 2012) or  $\text{Al}_2\text{O}_3$  (Deweale and Torrent, 2013). No correction was made for the thermal pressure effect.

The temperature in each experiment was first adjusted by levelling the laser power and coupling and focusing the lasers until both sides were at similar temperatures. Then the laser power was gradually increased on each side with a steady time increment until the target temperature at solidus, (Pradhan et al., 2015). Our goal was to induce melting but to keep the lowest degree of melting as possible. Therefore, as the laser power was ramped up, and after reaching the solidus temperature the experiment was finished and rapidly quenched by switching off the lasers. In few cases, we noticed a jump in the temperature to the solidus temperatures directly. All samples enclosed in the recovered gaskets containing the heated, recrystallized and melted basaltic lithologies were subsequently decompressed and kept under vacuum until further manipulation.

## 2.3. FIB sample preparation for SEM and TEM observations

The recovered DAC samples were transferred to a Zeiss Neon40EsB focused ion beam FIB-SEM system and characterized by Zeiss Ultra 55 field emission gun scanning electron microscope (FEG-SEM) and Jeol 2100F transmission electron microscope (TEM) at the IMPMC in

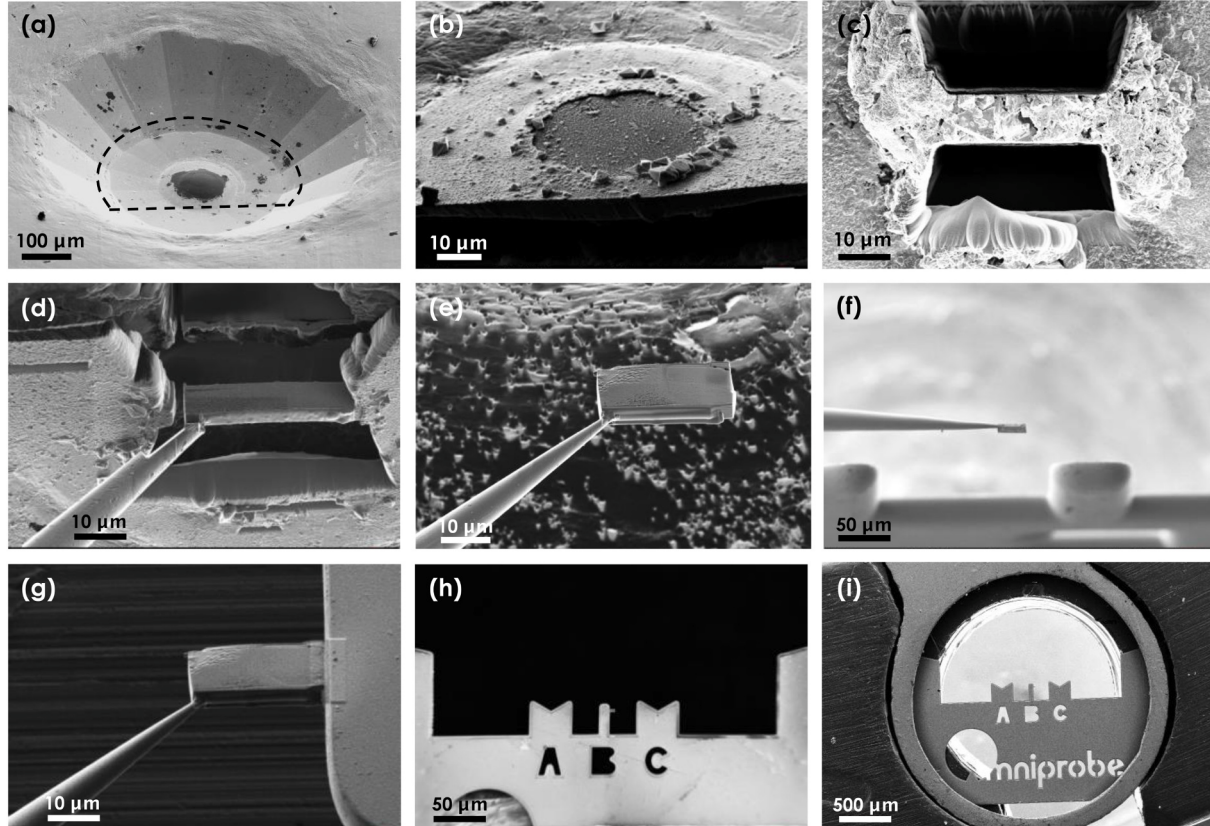


**Fig. 1.** Scanning electron images of the LH-DAC sample retrieval processes using focused ion beam (FIB) and scanning electron microscope (SEM). In short, the preparation starts with the sample decompression (a), Re-gasket cutting with laser driller (b), followed by large cuts with FIB (c) until the hotspot is found on both sides of the feature, Pt deposition on the thick lamella of interest (d), extraction of the lamella using micro-manipulating W-needle (e-f) and attachment to the TEM Cu-grid (g) for further thinning and cleaning on the TEM Cu grid (h) in order to later perform high quality chemical analyses using SEM (i), EMPA or TEM (more in the main text).

Paris, France. The flat and indented culet areas of the *Re*-gaskets were first cut out by femto-second laser in a shape of half-moon (Fig. 1a) and fixed on the edge of a clean and flat silicon wafer piece with C-conductive glue (Fig. 1b). The silicon wafer was then placed in the middle of the alumina SEM-stub covered with a Cu-conductive tape and subsequently carbon coated before FIB milling. On top of the selected region of interest we deposited a Pt stripe of about 2  $\mu\text{m}$  thickness. The FIB system at IMPMC allows electron imaging during the milling, enabling detection of the hot-spot area of the sample with high precision. When the quenched melts were exposed in an axial section from one side, the milling was continued from the other side. Thereby, we were able to locate the centre of the laser-heated hot spot, observe similar proportions of the quenched melt on both sides and prepare relatively thick (2–3  $\mu\text{m}$ ) and large (20–30  $\mu\text{m}$ ) section for extraction (Fig. 1c). The axial cuts were made through the entire thickness of the LH-DAC samples (15–30  $\mu\text{m}$ ) with the FIB gallium beam operating at different acceleration voltages (10, 5 and 2 kV). During the milling, we reduced the initial current of 10 nA for efficient and fast milling to about 1 nA current for more precise cutting of the sample surfaces, then reducing further to 100–200 pA current for fine polishing in order to decrease Ga-implantation from the gun. The pre-cut sample sections were covered with a deposited 2  $\mu\text{m}$  Pt strip and subsequently hitched to the remotely manipulated needle by Pt-welding (Fig. 1d), cut off the gasket and lifted from the *Re*-gaskets (Fig. 1e). Then, the sample was transferred and mounted onto a copper TEM grid, where final thinning and cleaning of the sample surface took place (Fig. 1f -h). The thick lamellae resulting from this preparation were used for imaging and chemical analyses, performed with the FEG-SEM. The copper grids with samples were mounted as flat as possible on the special STEM (Scanning Transmission Electron Microscopy) alumina holder (Fig. 1i) in order to achieve reliable chemical analyses with minimum background effect. All the chemical analyses were carried out at 15 kV accelerating voltage and 10–20 nA beam current.

Further preparation was then required to prepare the samples for the TEM observations. To achieve the electron transparency, we further thinned the extracted lamellae down to about 150–200 nm thickness. We decided to thin half of the hot-spot areas as the features were very symmetric and large enough for the detailed investigation with the TEM microscope.

The TEM observations were carried with a Jeol 2100 F transmission electron microscope operating at 200 kV, equipped with a field effect gun, a high-resolution UHR pole piece, a Gatan US4000 CCD camera, and an energy-dispersive X-ray (EDX) analysis system from Jeol, which allowed us to perform electron diffraction and imaging as well as elemental maps in STEM mode.

Analysis by FE-SEM has been used in the most recent LH-DAC metal-silicate partitioning studies (e.g. Pradhan et al., 2015; Tateno et al., 2018). We followed the same elaborated procedures of sample preparation (Fig. 1a-c) on all of our samples and we selected the centre of the heated area for lamella extraction and detail chemical analyses (SEM and TEM) samples. We used similar analytical conditions as described in the most recent publications to obtain elemental maps of the heated spots. However, it is worth mentioning that the electron microscopy analyses of the DAC samples need to be interpreted with caution and remain challenging due to potential analytical errors associated with the small size of the analysed material (e.g. Wade and Wood, 2012). The contribution of secondary fluorescence arising from the neighbouring phases, the effect of sample thickness and a relatively large beam size, unable to resolve all the quenched features, are examples of the potential sources of analytical errors. The sample thickness is especially crucial for analyses of low-atomic number silicates in which the primary X-Ray excitation depth is greater than that of metals. With the lamella extraction and careful thinning, we can provide more accurate results and improve the current understanding of the chemistry of observed features on the sub-micron scale. Doing analytical TEM on FIB sections on this system and finding essentially similar results makes us confident

that the results obtained here are robust.

### 3. Results

#### 3.1. XRD *in situ* in LH-DAC

The LH-DAC experiments were performed with basaltic starting compositions (Table 1) at around 60–70 and 90–100 GPa reaching temperatures above solidus (Andrault et al., 2014; Pradhan et al., 2015) in order to ensure melting, necessary for studying solid-liquid elemental partitioning and melting phase relations. Upon laser-heating, we commonly observed a distinct perturbation, in the form of temperature plateaus in the temperature vs. laser power curve. Temperature plateaus are well known as good indicators of melting, and are especially well resolved during invariant melting of metals but are also useful to determine the melting of various silicates (e.g. Shen and Lazor, 1995; Anzellini et al., 2013; Lord et al., 2014; Walter et al., 2015; Pradhan et al., 2015; Baron et al., 2017). As the starting material used in the present study and in Pradhan et al. (2015) was indeed the same natural basaltic glass (see Table 1), our melting experiments were performed in accordance with the Pradhan et al. (2015) protocol where the first appearance of a diffuse scattering together with a jump in T and further temperature plateau was employed as a melting criterion. Here, once we reached the solidus temperature reported by Pradhan et al., 2015, we rapidly quenched the experiments in order to study first melts and low-degree of melting in further sample recovery studies.

In Fig. 2 we present the typical diffraction patterns collected before and during laser heating at PETRA, DESY. All cold diffraction patterns (before even turning on the lasers) show no peaks as expected from an amorphous starting material, however we can detect the typical broad feature (so called ‘bump’) in the diffuse scattering pattern of the glassy starting material which suggests short-order structure of the silicate glasses around 9.0 2theta (Fig. 2). The signal from the KCl pressure transmitting media is observed before and throughout the heating cycles (Fig. 2 top). The amorphous Al<sub>2</sub>O<sub>3</sub> pressure medium gives no detectable signal in the room temperature (cold) diffraction pattern likely because of very small size of coherently diffracting domains of the deposited pressure medium. Once the lasers start to heat the sample, Al<sub>2</sub>O<sub>3</sub> recrystallizes and peaks corresponding to the pressure medium throughout the heating cycles can be observed (Fig. 2 bottom).

Collected XRD data allowed us to detect the co-existing phases, crystallizing from the amorphous basaltic glass during the experiment. In all high temperature and high pressure diffraction patterns we notice the immediate appearance of two main phases: bridgmanite ((Mg,Fe)SiO<sub>3</sub>) and Ca-perovskite (CaSiO<sub>3</sub>). With further heating, we detect crystallization of stishovite (SiO<sub>2</sub>) and of a CaFe-type Al-rich phase (see Fig. 2 top and bottom). These four crystalline phases have been also reported in all the previously published LH-DAC with *in-situ* XRD studies performed at similar pressure and temperature conditions (Andrault et al., 2014; Pradhan et al., 2015; Tateno et al., 2018).

Our results of XRD patterns in sub-solidus conditions are therefore in good agreement with Andrault et al., 2014; Pradhan et al., 2015, Tateno et al., 2018, although the experimental setups of all these experiments were different. Moreover, despite of using two different types of pressure media, we observed exactly the same phase relations in the diffraction patterns at high pressure-temperature conditions. In all experiments we also observed a jump in temperature at the solidus line; however, the fast quenching prevented us to detect the diffuse scattering signal from the small liquid portion generated during the experiment.

#### 3.2. Chemical mapping of concentric differentiated structures in the samples

A concentric structure with different layers of distinct chemical compositions (Figs. 3 and 4, Table 2) is observed in all the experiments. When we progressively approach the hot-spot area from the outside of

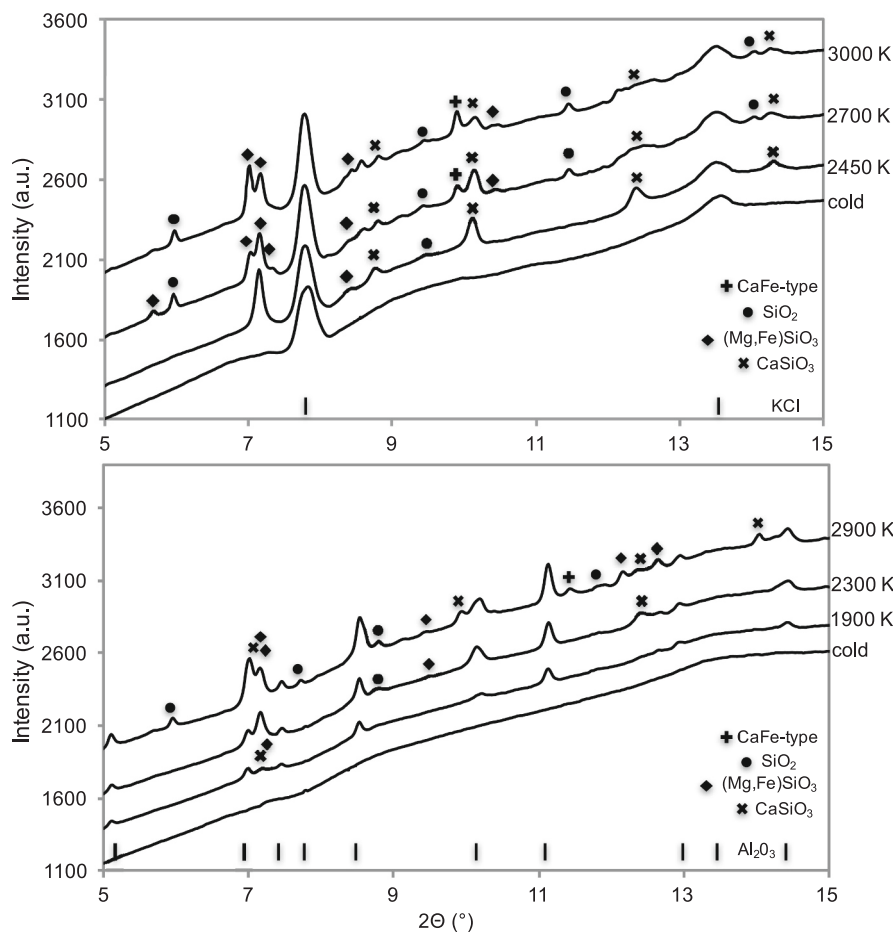


**Fig. 2.** *In situ* XRD patterns of the LH-DAC experiments made with the natural basalts using two different types of pressure medium: top: KCl - #12\_P9\_2 basalt at 65 GPa; bottom:  $\text{Al}_2\text{O}_3$  - #8\_Z3\_2 basalt at 65.5 GPa. The cold diffraction patterns were collected at room temperature and show no peaks from the sample except the distinctive bump from the amorphous glass.

the heated zone, we see in 2D a first outer ellipse growing when advancing the milling. It is composed of gains whose sizes increase towards the centre of the heated zone (Fig. 2 and more in Fig. S3 of supplementary materials). Then a second ellipsoid of the amorphous Ca-pv composition emerges and leads us to the centre of the last zone which itself contains two ellipsoids made of very homogeneous material without visible grains, and finally a small blob very iron-rich more or less at the center of the samples. The central blob is made of an Fe-S-O phase surrounded by an ellipsoid of a homogeneous phase highly enriched in iron and aluminum compared to the composition of the initial basaltic glass, and then the next ellipsoidal ring going towards the outside of the hotspot is made of a phase enriched in silicon and aluminum compared to the initial basaltic glass. Considering the strong compositional difference between the starting material and the materials in those two ellipsoids and in the central blob, we consider that they are melts constitutive of a central melt pocket that will be discussed further on. The quenched textures and general features of our recovered samples are similar to those observed in previous basaltic melting studies (e.g. Pradhan et al., 2015; Tateno et al., 2018). In Fig. 3 we summarise the typical BSE electron images and SEM elemental maps of the major elements: Si, Mg, Fe and O. More elemental distribution maps of Al, Na, Ti, S, K and Cl can be found in the supplementary materials (Appendix A). We find no contamination from the surrounding medium as the small heated area has been protected by the unreacted glassy sample from the pressure-medium and therefore even at high temperature neither reaction nor elemental diffusion has occurred. We also do not see the typical effects of the Soret diffusion (Sinmyo and Hirose,

2010), where Fe would escape the hottest area in the centre of the laser-heated spot.

In general, in all experiments performed around 60–70 GPa (Fig. 2a-b) we notice that the central melt pool consists of the three described component (Fe-O-S blob, Fe-enriched and Fe-poor silicate melts). However, in few higher-pressure experiments above 100 GPa (Fig. 2c) the melt pool exhibits more homogeneous appearance but overall similar elemental partitioning characteristics. In few cases, in co-existence with the melt pocket we have also captured crystals of stishovite or Ca-perovskite trapped in the melt matrix (Fig. 2b).

In Fig. 4 and Appendix B Energy Dispersive X-ray maps acquired at high magnification in the TEM can be found together with electron images of the whole reacted areas. Based on this more detailed TEM observations we confirm that the quenched Fe-poor melt is usually very homogeneous and fine-grained on all scales (Fig. 4b) with a glassy appearance, suggesting rapid quenching of the silicate material. The quenched texture of the Fe-rich melt is also chemically very homogeneous (like in Fig. 3a and b) but in the nano-scale observations we notice needle-like microstructures at the boundary with the Fe-poor melt and more nano-scale quenched textures (Fig. 4b). As revealed by TEM, the Fe-blobs in the centre consist actually of FeO and FeS domains (Fig. 4a) and the boundary with Fe-rich melt is remarkably distinctive. Similar metal alloys melts have been previously observed and have been featured in run products from large volume press (LVP) experiments (e.g. O’Neil et al., 1998; Ricolleau et al., 2011; Siebert et al., 2011) and previous LH-DAC as well (e.g. Fiquet et al., 2010; Frost et al., 2010; Siebert et al., 2012). Around the melt pool, the  $\text{CaSiO}_3$  ring, which in

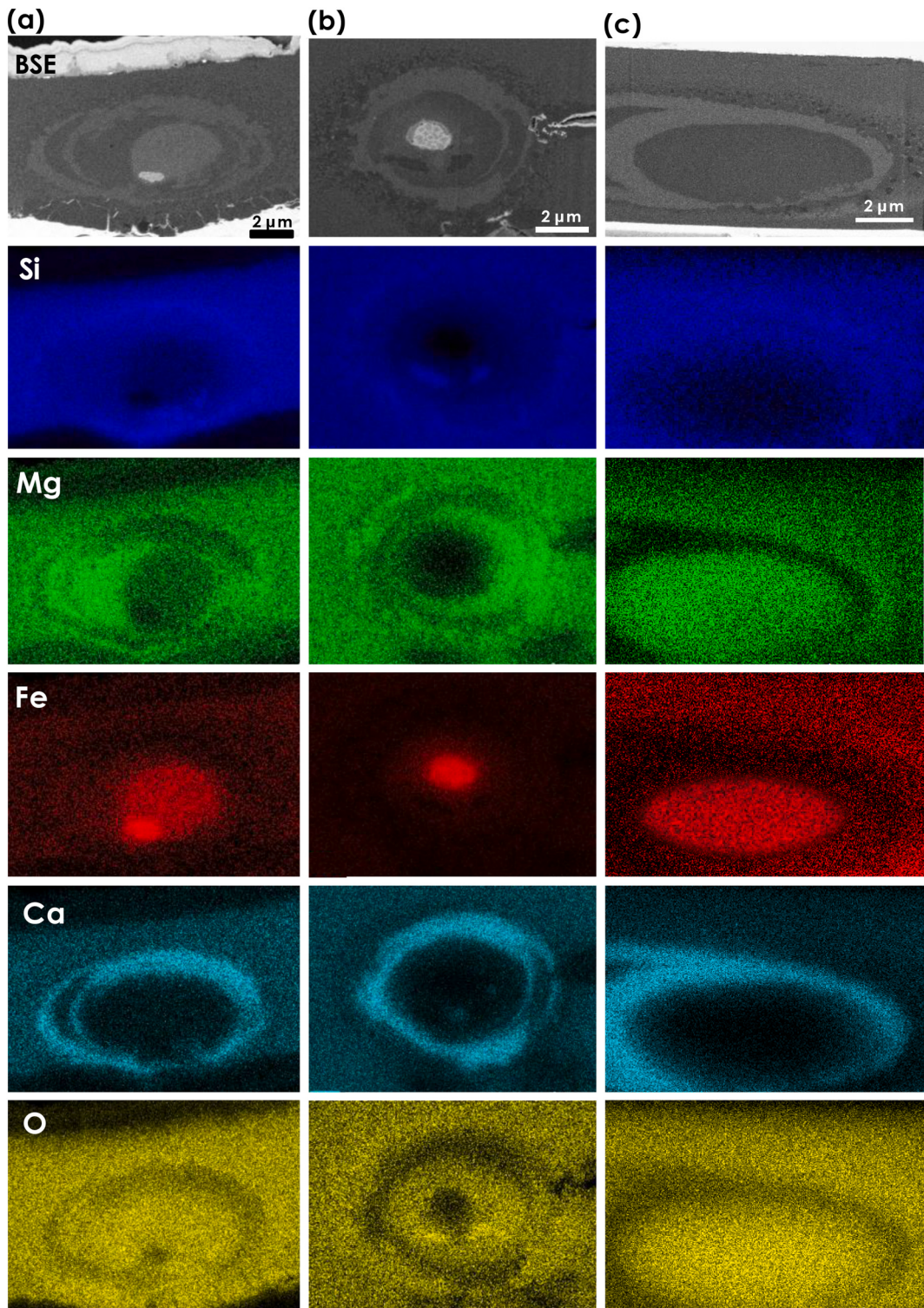


**Fig. 3.** EDX elemental maps and BSE/SE images of the melting experiments of natural basalt, (a) – #12\_P9\_2 65 GPa, (b) – #8\_M3\_1 65.5 GPa, (c) – #6\_P6\_2 101 GPa. On the Ca-map we see the Ca-pv ring encapsulating the melt components, On the Fe-map we can distinguish the metal blobs for samples at lower pressures ans the Fr-rich melt. On the Mg-map, the Fe-poor melt shows Mg-rich zone.

SEM pictures resembles a glassy homogeneous texture but in the TEM images, as in Fig. 4c, we can detect the nano-scale grains with  $\text{CaSiO}_3 - \text{SiO}_2$  domains. In contact with this  $\text{CaSiO}_3$  large areas, the basalt starting glassy material has recrystallized into  $(\text{Mg},\text{Fe})\text{SiO}_3$  perovskite (bridgemanite)  $\text{CaSiO}_3$  – perovskite (amorphized) and  $\text{SiO}_2$  (stishovite). In the recrystallized subsolidus zone examined by TEM, we have also detected distinctive crystals of Calcium Ferrite (CF-type) Na and Al-rich phase in

sub-micron scale which can be found in the supplementary materials (Appendix C). These phases have already been described in previous experiments on similar samples (Ricolleau, 2011). All of the subsolidus phases found in the FIB sections have also been confirmed in the X-ray diffraction patters (Fig. 2).

Carbon contamination through diffusion from diamond anvils was not observed, and the relatively high totals of the microprobe analyses

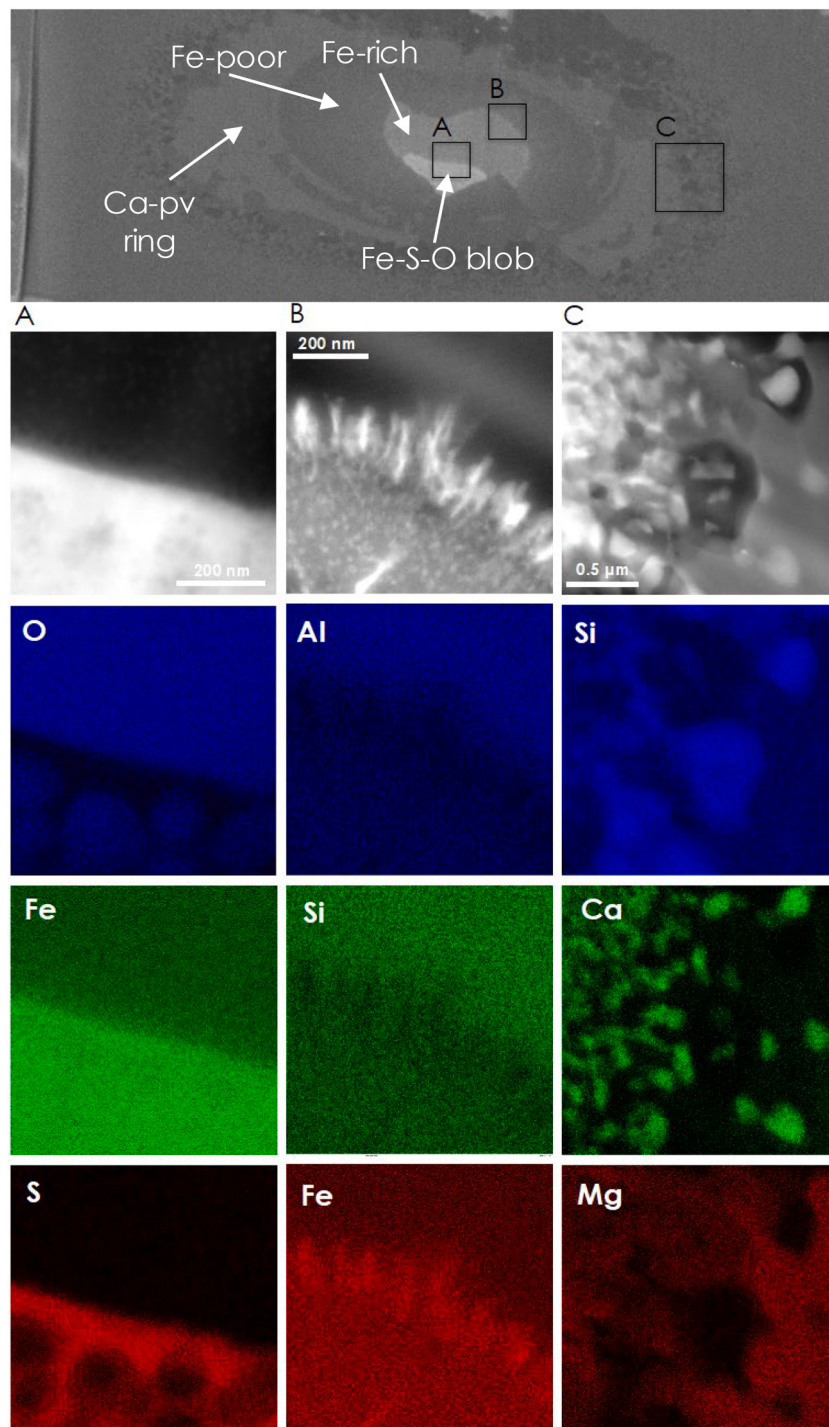


**Fig. 4.** TEM STEM elemental maps and electron images of the melting experiment of natural basalt (#2\_basalt at 64 GPa). The three regions of interest show three types of interfaces between A: metallic melt and Fe-rich melt; B: Fe-rich melt and silicate melt; C: Ca-perovskite and sub-solidus recrystallisation of a basaltic phases:  $\text{SiO}_2$  stishovite,  $(\text{Mg}, \text{Fe})\text{SiO}_3$  bridgemanite and small grains of  $\text{CaSiO}_3$ .

suggest very low C-contribution. This was probably a result of the pressure-medium acting as a chemical barrier between the basaltic glass and diamond anvils.

From the SEM and TEM chemical observations on the micro and nanoscale, respectively, we have extracted the chemical compositions of coexisting phases in the hotspots, summarized in Table 2. We also compare analyses made on two samples which were melted at similar pressure ( $\sim 65$  GPa) in experiments performed using either  $\text{Al}_2\text{O}_3$  or KCl pressure medium. We notice no significant difference in the chemical

compositions of all the prominent components of the experimental assembly, the Fe-poor and Fe-rich melts, Ca- and Mg-perovskites (Table 2). It is however worth mentioning that due to the small size of the crystalline phases (e.g. MgPv on the outskirt of the large Ca-pv layer in the sample #12 in KCl) the analyses made by the EDX-TEM on the very thin lamellas provide better resolved chemical contrast of the nano-scale features (e.g. Fig. 4) than EDX-SEM data (Fig. 3) which were made on thicker lamellas, where the effect of the excitation depth may alter the observations. On the other side, the EDX-SEM analyses are calibrated

**Table 2**

Chemical composition of coexisting phases in the hotspots.

Run	#8 in Al <sub>2</sub> O <sub>3</sub>				#12 in KCl			
Pressure	65.5 GPa				65 GPa			
Phase	Fe-poor	Fe-rich	Ca-pv	Mg-pv	Fe-poor	Fe-rich	Ca-pv	Mg-pv
SEM	SiO <sub>2</sub>	43.40	28.99	52.33	42.83	38.15	33.04	52.09
wt%	TiO <sub>2</sub>	2.17	4.63	–	1.21	2.09	5.83	1.24
	Al <sub>2</sub> O <sub>3</sub>	25.66	23.37	7.09	16.09	30.10	20.50	5.87
	FeO	11.02	33.61	6.19	7.55	15.55	34.61	5.02
	MgO	13.56	4.30	4.10	17.99	7.59	1.76	5.98
	CaO	3.05	3.02	30.05	11.10	2.77	1.44	27.91
	Na <sub>2</sub> O	1.21	2.14	–	2.44	2.99	2.75	1.81
	Total:	100.07	100.06	99.76	99.21	99.24	99.93	99.81
TEM	O	61.81	41.14	44.48	58.89	64.46	60.61	55.64
at.%	Na	0.53	1.07	0.32	0.75	1.07	1.27	0.49
	Mg	6.43	1.52	2.03	10.07	4.03	0.29	2.5
	Al	11.60	7.19	1.73	7.81	12.49	8.33	2.47
	Si	11.87	7.2	14.65	15.60	11.58	8.50	20.78
	Ca	0.71	0.98	10.91	0.92	0.96	0.79	15.33
	Ti	0.61	1.32	0.65	–	0.64	2.79	0.64
	Fe	6.44	19.06	5.21	5.96	4.76	17.43	2.14
	Cu	–	20.35	20.02	–	–	–	–
	Total	100.00	100.00	100.00	100.00	100.00	100.01	100.00

with standards and therefore provide more reliable quantitative values of chemical composition of phases, in weight % of oxides than EDX-TEM data in atomic % (Table 2).

The metallic blobs also show same chemical and textural characteristics despite the difference in the used pressure medium (Fig. 4 and Appendix B, Fig. S2). Regions of S and O-enrichment can be distinguished in the TEM images and chemical maps. An example of the metal blob chemical analysis can be found in the Appendix B (Table S1) from the sample synthesized in Al<sub>2</sub>O<sub>3</sub> at 65.5 GPa.

In addition, we have also summarized the experimental chemical data obtained in the previously published literature in Appendix D and we see similar chemical compositions of all the major crystalline phases, however in order to directly compare the melt compositions we suggest to use a model which we describe later (see Table 3).

### 3.3. Remarks on the pressure medium (PM)

In order to understand further effects due to pressure medium on LH-DAC melting experiments we used KCl or amorphous Al<sub>2</sub>O<sub>3</sub> discs as a pressure medium, pressure calibrant, and thermal insulator. Based on our *in situ* XRD and elemental maps of the recovered samples we notice that using a thin layer of pressure medium, either KCl or Al<sub>2</sub>O<sub>3</sub>, does not interfere with the crystallization sequence and partitioning behaviour of the elements. No matter what material we used as the pressure medium, the diffraction patterns of the heated basaltic samples show the same phases crystallizing from the homogeneous glass. Experiments with KCl were particularly successful as sodium chloride structure is cubic with well identified peaks that did not overlap with the X-ray diffraction signal from the sample. In case of an Al<sub>2</sub>O<sub>3</sub> pressure medium, the heated

amorphous glass crystallized during LH-DAC experiment, which on one hand serves as a robust internal pressure calibrant but on the other hand strongly diffracts, masks signal from the sample and makes the interpretation of XRD patterns more challenging. The laser heating has been very efficient as the pressure medium was acting as an efficient thermal insulator, preventing the heat loss through the conductive diamond anvils. A lot of attention has to be made to the post-experimental preparation of samples because the heating spot has to be kept smaller than the size (thickness) of the glassy silicate sample, *i.e.* the hot spot ideally is still surrounded by unreacted glassy zone which we have documented further in the supplementary materials (Appendix E). As soon as there was a mechanical contact between the melt and pressure medium a reaction can occur which contaminates the primary starting composition and influences the partitioning relations. In the perspective of previous LH-DAC experiments, although in the Andrault et al., 2014 KCl pressure medium has also been used, we have obtained results closer to the more recent studies in which no pressure transmitting media was used, and the region of interest has been preserved within the bulk unheated glassy starting material (Pradhan et al., 2015; Tateno et al., 2018).

## 4. Discussion

### 4.1. Calcium silicate perovskite as the liquidus phase in melting of basaltic compositions

In all our experiments, we report a concentric structure made of successive rings with a geometry of revolution ellipsoids (Fig. 5) which obviously correspond to the hot spot of the laser with less efficient heating when approaching the diamond in any plane containing the laser axis (Fig. 5). In all planes the structure of the samples is evolving isotropically because the projection of the hot spot is an elongated perpendicular to the compression axis sphere, with a gaussian temperature profile. Outside of the elliptical hot spot, one finds unreacted glassy starting material, then transformed material with increasing grain sizes when moving towards the center of the samples (*e.g.* Fig. 5d and e). This sequence is most likely associated with a subsolidus assemblage in those areas of the laser-heated spot in which temperature was not sufficient for melting. Then the other inner rings or ellipsoids have bulk chemistries very different from the starting material and are most likely associated to melting. The outermost of these rings is dominated by a composition close to CaSiO<sub>3</sub>. This leads us to state that CaSiO<sub>3</sub> perovskite (cpv) is the last solid phase to melt (liquidus phase) and thus the

**Table 3**

Modelled melt compositions.

	#8	#12
fraction	Fe-poor	0.56
	Fe-rich	0.44
SEM	SiO <sub>2</sub>	37.06
wt%	TiO <sub>2</sub>	3.25
	Al <sub>2</sub> O <sub>3</sub>	24.65
	FeO	20.96
	MgO	9.47
	CaO	3.04
	Na <sub>2</sub> O	1.62
	Total	101.05
		100.31

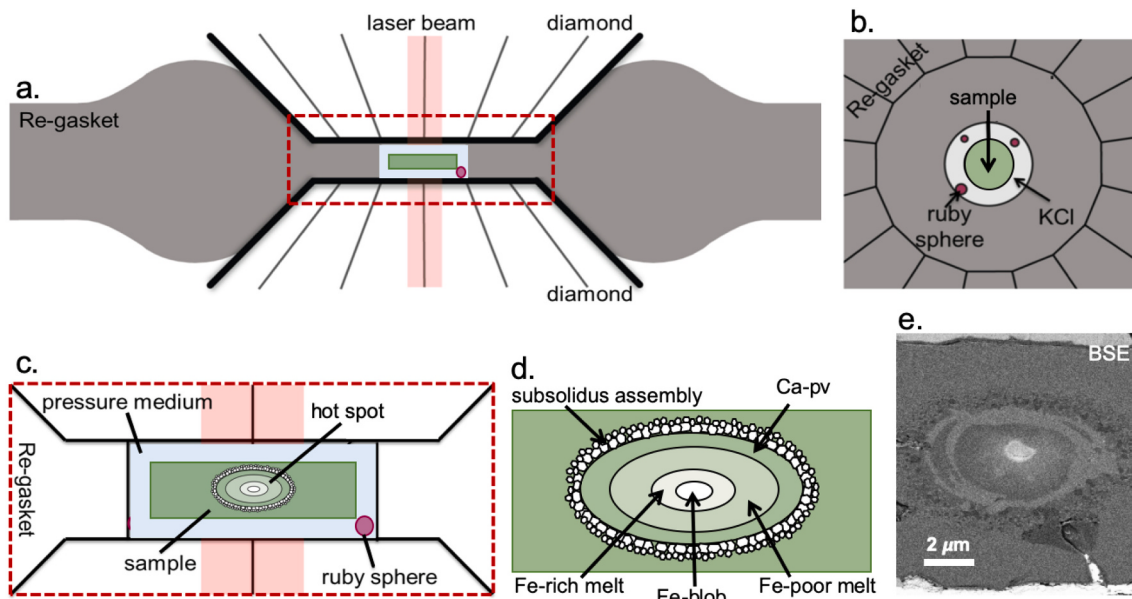


**Fig. 5.** Schematic diagrams of the LH-DAC experimental assembly: (a) with respect to the position of diamonds, Re-gasket, laser beams (red shaded), (b) a top view of the experimental setup in the Re-gasket (c) a typical cross section showing the experimental setup with a sample that has been heated and melted at high pressure, surrounded by  $\text{KCl}/\text{Al}_2\text{O}_3$  pressure medium and ruby sphere inside the sample chamber of the pre-indented Re-gasket (d) magnified view of the typical result of the high pressure and high temperature experiments after quenching showing the observed and described in this study melt structures (Fe-poor, Fe-rich and Fe-blob), liquidus phase (Ca-pv) and the subsolidus assembly: recrystallisation of a basaltic phases surrounded by unreacted glassy sample (e) BSE image of the hot spot area in one of our experiments, for comparison. (For interpretation of the references to colour in this figure legend, the reader is referred to the web version of this article.)

first to crystallize in a crystallization sequence. It is very likely that once formed upon temperature elevation, the melt migrates towards the center of the sample (see discussion below) forming the innermost ellipsoidal rings and blob. Previously published studies on basaltic melts compositions in the lower mantle pressure regime agree that the crystallization sequence is first cpv as the liquidus phase, followed by stishovite (stv) or modified stishovite ( $\text{CaCl}_2$ -structured) and then bridgemanite bm (Andrault et al., 2014; Pradhan et al., 2015; Tateno et al., 2018). This behaviour does not drastically change over a large pressure range.

At pressures exceeding 108 and 123 GPa, the crystallization sequence of a basaltic melt has been reported to be cpv-bm-silica and cpv-pbm-silica, respectively (Tateno et al., 2018). Seifertite ( $\text{SiO}_2$  with  $\alpha\text{-PbO}_2$  structure) likely replaces modified stishovite ( $\text{CaCl}_2$ -structured silica) as the silica phase near the solidus at lowermost mantle conditions. At lower pressures, based on multi-anvil press experiments, Hirose and Fei (2002) found that cpv and stishovite crystallize almost simultaneously at 23–24 GPa, but that cpv is clearly the liquidus phase, preceding stishovite at slightly higher pressures of 25–28 GPa.

For a comparison, the crystallization sequence of natural peridotite at pressures above 30–40 GPa is different, with bridgemanite (bm) as the liquidus phase, followed by ferropericlase (fp) and then cpv as a solidus phase (Fiquet et al., 2010; Andrault et al., 2011; Tateno et al., 2014; Nomura et al., 2014; Nabe et al., 2021). This clearly distinguishes the consequences of melting of the two most discussed Earth's mantle lithologies.

#### 4.2. Iron enrichment of melts

We subsequently used electron microscopy on recovered run products to better understand the melting phase relations and quenched textures captured during the high-pressure and high temperature experiments. The Fe–S and Fe–O phases observed in the center of the samples (Figs. 3 and 4) are most likely quenched textures of a Fe–S–O metallic melt. The abundance of this metallic melt is very low. The

most likely interpretation of this melt is that it could be related to the products of the bridgemanite disproportionation reaction (e.g. Frost et al., 2004) and coalesce in the centre of the experimental charge as melting develops (see discussion of melt migration below).

Then moving outwards from the sample centre, two ellipsoidal zones with very different chemical composition than that of the starting material are observed, corresponding to melts both enriched in Al, one of the two melts being very depleted in Si and very enriched in Fe (Table 2). It is possible that these two melts correspond to two liquid phases appearing successively during the temperature rise and then migrating immediately once formed, or to an immiscibility in the liquid state. It is interesting to combine the compositions of these two liquids using a first rough approximation which consists in ponderating their compositions by their surface proportions. In Table 3 we present modelled melt compositions of two similar samples melted and quenched at around 65 GPa but embedded in two different pressure media (#12\_P9\_2 in  $\text{Al}_2\text{O}_3$  and #8\_M3\_1 in KCl). Using the BSE images and chemical maps (Fig. 3) we estimate the fraction of the Fe-poor and Fe-rich melt and we use the chemical compositions of the two components (presented in Table 2). We thus obtain an average liquid resulting from basalt fusion (Table 3) whose composition is strongly enriched in Al and Fe compared to the composition of the initial basalt glass. This is consistent with the results of several previous studies which showed that upon high pressure melting of basalts, the silicate melts are enriched in FeO relative to the solid starting material (see Fig. 3) reflecting preferential partitioning of FeO into the melt (e.g. Corrige et al., 2008; Tateno et al., 2014; and Pradhan et al., 2015). Andrault et al., 2014 showed results in which melts are Si-enriched at the highest pressures of the lower mantle (120 GPa), however in the intermediate pressures (38–80 GPa) such enrichment is not evident. Considering the segregation of melts observed in our experiments, we propose that an iron-rich melt might have remained undetected in Andrault et al., 2014 highest pressure experiments due to type of sample preparation and chemical observation made from the top surface, without exposing the centre of the hotspots. In our approach of exposing the very centre of the hotspots, we gain a better control of the

complex geometry of quench features. We used the EDX-SEM chemical compositions of the Fe-poor and Fe-rich phases described above (Table 2).

Mentions of liquid silicate immiscibilities are uncommon in very high pressure melting studies, which we also confirm in our highest pressure experiment at 101 GPa (Fig. 3c). However, liquid immiscibilities in basaltic compositions have often been reported, albeit at lower pressures (Vincenzi et al., 1995; Vekslar et al., 2007). The complexity of LH-DAC features and therefore understanding of the melt segregation and concentric layers is therefore a priority.

#### 4.3. Understanding the melt segregation and concentric layers

The quenched samples of concentrical features starting from the center: Fe-O-S melt, Fe-rich melt, Fe-poor melt, CaSiO<sub>3</sub> ring (liquidus phase), solidus assemblage, untransformed basaltic glass (Figs. 3 and 4). Similar observations of onion-rings have been made in previous basalt melting or peridotite melting studies at high pressure in laser heated diamond-anvil cell experiments. What are possible interpretations of these structures?

The intense laser heating induces instantaneously huge gradients of thermal pressure P and temperature T (of orders 0.1 GPa/1 μm and 100 K/1 μm). A possible source of segregation of phases initially mixed could be due to the difference in their mechanical strengths. If one phase is less viscous than the other, its pressure will be more homogeneous. The interface between the phases of different properties will then influence the local pressure environment leading the more viscous phase to the centre and expulsing the less viscous phase away from the highest-pressure zone. This compaction mechanism should drain the less viscous phase from the hotspot (McKenzie, 1984; Ricard et al., 2001). This would yield a separation of phases with the most viscous phase (probably the silicate melt most depleted in Fe) at the centre, that appears opposite to what we observed.

The surface tension between phases,  $\sigma$  is certainly a major force at the micrometric scale  $r$  of these experiments as the ratio between surface tension and gravity forces is  $\sigma/\rho_0 g r^2 > 1$ . The effect of surface tension is twofold. A first and usual effect of surface tension is associated to the curvature of the interface separating phases. This favours the formation of large bubbles by coalescence of smaller bubbles until the two phases self-separate (like oil and water). This mechanism should therefore lead to the separation of the different immiscible phases but cannot explain the embedded final position of these various phases.

A second effect of surface tension is related to the inhomogeneity of the temperature. This induces forces, called Marangoni forces (Marangoni, 1871), related to surface tension gradients rather than to interface curvature. These forces tend to drive the phase interfaces in the direction where the surface tension is lower. They act on the bubbles of the low viscosity phase and drive them to the center of the hotspot as surface tension is lower at high temperature (Young et al., 1959; Ricard et al., 2021). This effect is related to the product of the temperature derivative of surface tension  $\sigma'$  times the temperature gradient. There are not many experiments measuring  $\sigma'$  for phases relevant to the pressure and temperature conditions of the experiment but Terasaki et al. (2012) suggests  $\sigma' \approx -2 \text{ mN m}^{-1} \text{ K}^{-1}$ . Such a value implies that the self-separation and the Marangoni forces have similar amplitude as their ratio  $\sigma'/(-\sigma' T) \approx 1$ . This importance of the Marangoni force in this experiment is of course due to the huge temperature gradient that is imposed.

It seems therefore that Marangoni forces with the likely conditions that the surface tension between metal and silicates is larger than between the metal-rich and metal-poor silicate melts, are able to segregate the liquid phases in the order indicated by the experiment. This segregation is helped by the more common aspect of capillary forces, leading to self-separation.

#### 4.4. Application of the observations in the Earth's mantle

Considering our new experimental data on melting phase relations and elemental partitioning at high pressure and temperatures relevant to the deep Earth, and in agreement with Pradhan et al., 2015, Tateno et al., 2018, we have confirmed that basaltic material which happens to reach the deepest part of the lower mantle will melt. The melting temperature of basaltic lithologies determined by Pradhan et al., 2015 and used in this work to target solidus temperatures for study of early melts (low degree melting) has been confirmed in our experiments. The Fe-, Al-, and Mg-rich melt will segregate leaving highly refractory Ca-pv behind which will lead to accumulation of these components at the bottom of the Earth's mantle. Such melts might potentially be the source of the ultra-low velocity zones (ULVZs) which have been detected locally on the edges of the large low-shear velocity provinces (LLSVPs) which dominate the D'' zone, just above the core-mantle boundary (CMB).

The density and viscosity of the melts and crystal residuals at the extreme conditions of the CMB need to be studied further to understand their role in the overall structure, compositions, dynamics and evolution of the Earth's interior, potentially using novel experimental methods and atomistic calculations.

#### 5. Conclusions

Reaching the high pressure-temperature conditions of the Earth's deep interior and particularly performing *in situ* experiments at synchrotron facilities provides the only way to sample and reconstruct the melting phase relations and crystallization sequences relevant to planetary geodynamics. Adding *ex situ* investigations of quenched melting experiments enables detailed solid-liquid elemental partitioning investigations. Studying basaltic samples at lower mantle conditions is therefore a shortcut into understanding the past events and present-day mantle heterogeneities, which are linked with the subduction zones.

Using LH-DAC experiments combined with *in situ* X-Ray Diffraction measurements at the synchrotron, we studied crystallization and melting of natural basaltic lithologies at 60–100 GPa and up to 4000 K. We decompressed and recovered samples to perform *ex situ* investigation using focused ion beam techniques (FIB) and electron microscopies (SEM and TEM) to map and visualize the heated zones and understand the chemical partitioning of elements induced by melting under high pressures and temperatures. We used pressure media (KCl and amorphous Al<sub>2</sub>O<sub>3</sub>) to test the influence of this parameter on the results.

In the studied pressure range, all the diffraction patterns contained bridgmanite and Ca-perovskite crystallizing as major phases already at relatively low temperatures, with the increasing temperature crystallization of Si-phases (mainly stishovite) and CF-type Al- and Na-rich phase has been detected. The melting was assigned to the sudden jump in the temperature measurement around the solidus temperature in agreement with the Pradhan et al., 2015 melting curve.

Based on our chemical observations, we notice distinctive 'onion like' shells of various experimental products. In the middle, the melts are Fe-, Mg- and Al-rich and consist of Fe-poor and Fe-rich domains with small FeO + FeS metallic blobs linked with bridgmanite disproportionation reaction. The liquidus phase is Ca-perovskite, creating rings of nano-crystalline CaSiO<sub>3</sub> that encapsulate the melt pool throughout the studied pressure range. In co-existence with the melt, we have also captured crystals of stishovite, Ca-perovskite. Towards the colder area we observe the characteristic sub-solidus assembly of sub-micron grains of bridgmanite, Ca-pv, stishovite and CF-structure Al- and Na-rich phase. No effect of the used pressure media on the melting phase relations, melting and elemental partitioning is noted. However, the laser-heating spot must be smaller than the thickness of the starting material to avoid contamination and preserve the unreacted glassy starting material around the hotspot.

Due to the complexity of the structure and composition of the melt

pockets presented in LH-DAC experiments we have investigated the possible physical explanation of their formation. We described the potential impact of the temperature and pressure gradients, surface tension and Marangoni forces on the formation of the heterogeneous melt zones. It appears that the conjunction of capillary forces and temperature dependence of surface tension offer the best explanation of the observed arrangement of segregated melt phases.

Reflecting our experimental observation with the global view of the subducted basaltic lithologies back in the lower mantle we confirm that if basaltic material melts under lower mantle presumably in the deepest parts of the lower mantle close to the Core Mantle Boundary, Fe rich melt will be segregated downward.

## Author statement

**Marzena A. Baron:** Conceptualization, Methodology, Data curation, Formal analysis, Investigation, Methodology, Project administration, Visualization, Writing - original draft, Writing - review and editing.

**Guillaume Fiquet:** Conceptualization, Funding acquisition, Data curation, Writing- Original draft preparation, Supervision.

**Guillaume Morard:** Investigation, Writing- Original draft preparation.

**Francesca Miozzi:** Investigation, Writing- Reviewing.

**Béatrice Doisneau:** Technical support.

**Imène Esteve:** Technical support.

**Anna S. Pakhomova:** Investigation.

**Yanick Ricard:** Conceptualization, Validation, Writing- Reviewing and Editing.

**François Guyot:** Conceptualization, Writing- Reviewing and Editing, Supervision.

## Declaration of Competing Interest

The authors declare that they have no known competing financial interests or personal relationships that could have appeared to influence the work reported in this paper.

## Acknowledgements

The research has been founded by the European Research Council (ERC) under the European Union's Horizon 2020 research and innovation Programme (grant agreement 670787, PlanetDive). The Focused Ion Beam (FIB) and Scanning Electron Microscope (SEM) facility at IMPMC are supported by Région Ile de France grant SESAME 2006 N°I-07-593/R, INSU-CNRS, Institut de Physique (INP)-CNRS, University Pierre et Marie Curie-Paris 6, and by the French National Research Agency (ANR) grant ANR-07-BLAN-0124-01. Femtosecond laser micromachining at the Institut de Minéralogie de Physique des Matériaux et de Cosmochimie (IMPMC), Paris, has been developed and realized by the "Cellule Project" with the financial support of ANR 2010-JCJC-604-01. The *in-situ* XRD measurements and LH-DAC experiments were carried out at beamline P02.2 at PETRA III at DESY, which is part of the Helmholtz Association (HGF).

## Appendix A. Supplementary data

Supplementary data to this article can be found online at <https://doi.org/10.1016/j.pepi.2022.106938>.

## References

- Andrault, D., Bolfan-Casanova, N., Nigro, G.L., Bouhif, M.A., Garbarino, G., Mezouar, M., 2011. Melting curve of the deep mantle applied to properties of early magma ocean and actual core-mantle boundary. *Earth Planet. Sci. Lett.* 304, 251–259.
- Andrault, D., Pesce, G., Bouhif, M.A., Bolfan-Casanova, N., Hénot, J.-M., Mezouar, M., 2014. Melting of subducted basalt at the core-mantle boundary. *Science* 344 (6186), 892–895.
- Anzellini, S., Dewaele, A., Mezouar, M., Loubeyre, P., Morard, G., 2013. Melting of iron at Earth's inner core boundary based on fast X-ray diffraction. *Science* 340 (6131), 464–466.
- Baron, M.A., Lord, O.T., Myhill, R., Thomson, A.R., Wang, W., Trønnes, R.G., Walter, M.J., 2017. Experimental constraints on melting temperatures in the MgO-SiO<sub>2</sub> system at lower mantle pressures. *Earth Planet. Sci. Lett.* 472, 186–196.
- Boukaré, C.E., Ricard, Y., Fiquet, G., 2015. Thermodynamics of the MgO-FeO-SiO<sub>2</sub> system up to 140 GPa: application to the crystallization of earth magma ocean. *J. Geophys. Res.* 120 (9), 6085–6101.
- Corgne, A., Keshav, S., Wood, B.J., McDonough, W.F., Fei, Y., 2008. Metal-silicate partitioning and constraints on core composition and oxygen fugacity during earth accretion. *Geochim. Cosmochim. Acta* 72, 574–589.
- Deweale, A., Torrent, M., 2013. Equation of state of  $\alpha$ -Al<sub>2</sub>O<sub>3</sub>. *Phys. Rev. B* 88, 064107.
- Deweale, A., Belonoshko, A.B., Garbarino, G., Occelli, F., Bouvier, P., Hanfland, M., Mezouar, M., 2012. High-pressure-high-temperature equation of state of KCl and KBr. *Phys. Rev. B* 85, 214105.
- Elkins-Tanton, L.D., 2012. Magma oceans in the inner solar system. *Annu. Rev. Earth Planet. Sci.* 40, 113–139.
- Fiquet, G., Auzende, A.L., Siebert, J., Corgne, A., Bureau, H., Ozawa, H., Garbarino, G., 2010. Melting of peridotite to 140 GPa. *Science* 329, 1516–1518.
- Frost, D.J., Liebske, C., Langenhorst, F., McCommon, C.A., Trønnes, R.G., Rubie, D.C., 2004. Experimental evidence for the existence of iron-rich metal in the Earth's lower mantle. *Nature* 428, 409–412.
- Frost, D.J., Asahara, Y., Rubie, D.C., Miyajima, N., Dubrovinsky, L.S., Holzapfel, C., Ohtani, E., Miyahara, M., Sakai, T., 2010. The partitioning of oxygen between the Earth's mantle and core. *J. Geophys. Res.* 115, B02202.
- Fukao, Y., Obayashi, M., 2013. Subducted slabs stagnant above, penetrating through, and trapped below the 660 km discontinuity. *JGR Solid Earth* 118 (11), 5920–5938.
- Garnero, E.J., McNamara, A.K., 2008. Structure and dynamics of Earth's lower mantle. *Science* 320, 626–628.
- Hirose, K., Fei, Y., 2002. Subsolidus and melting phase relations of basaltic composition in the uppermost lower mantle. *Geochim. Cosmochim. Acta* 66, 2099–2108.
- Hirose, K., Fei, Y., Ma, Y., Mao, H.-K., 1999. The fate of subducted basaltic crust in the Earth's lower mantle. *Nature* 397, 53–56.
- Labrosse, S., Hernlund, J.W., Coltice, N., 2007. A crystallizing dense magma ocean at the base of the Earth's mantle. *Nature* 450, 866–869.
- Lay, T., Hernlund, J., Buffett, B.A., 2008. Core-mantle boundary heat flow. *Nat. Geosci.* 1, 25–32.
- Liebske, C., Frost, D.J., 2012. Melting phase relations in the MgO-MgSiO<sub>3</sub> system between 16 and 26 GPa: implications for melting in Earth's deep interior. *Earth Planet. Sci. Lett.* 345–348, 159–170.
- Liermann, H.P., Konópková, Z., Morgenroth, W., Glazyrin, K., Bednarcik, J., McBride, E.E., Petitgirard, S., Delitz, J.T., Wendt, M., Bican, Y., Ehnes, A., Schwark, I., Rothkirch, A., Tischer, M., Heuer, J., Schulte-Schrepping, H., Kracht, T., Franz, H., 2015. The extreme conditions beamline P02.2 and the extreme conditions science infrastructure at PETRA III. *J. Synchrotron Radiat.* 22, 908–924.
- Lord, O.T., Wann, E.T.H., Hunt, S.A., Walker, A.M., Santangeli, J., Walter, M.J., Dobson, D.P., Wood, I.G., Vočadlo, L., Morard, G., Mezouard, M., 2014. The NiSi melting curve to 70 GPa. *Phys. Earth Planet. Inter.* 233, 13–23.
- Mao, H.K., Xu, J., Bell, P.M., 1986. Calibration of the ruby pressure gauge to 800-kbar under quasi-hydrostatic conditions. *J. Geophys. Res. Solid Earth* 91, 4673–4676.
- Marangoni, C., 1871. Ueber die ausbreitung der tropfen einer flüssigkeit auf der oberfläche einer anderen. *Ann. Phys.* 219 (7), 337–354.
- McKenzie, D., 1984. The generation and compaction of partially molten rock. *J. Petrol.* 25, 713–765.
- McNamara, Allen K., Garnero, Edward J., Rost, Sebastian, 2010. Tracking deep mantle reservoirs with ultra-low velocity zones. *Earth Planet. Sci. Lett.* 299 (1–2).
- Morard, G., et al., 2017. Fe-FeO and Fe-Fe3C melting relations at Earth's core-mantle boundary conditions: Implications for a volatile-rich or oxygen-rich core. *Earth Planet. Sci. Lett.* 473, 94–103.
- Nabei, F., Badro, J., Boukarié, Ch.-É., Hébert, C., Cantoni, M., Borensztajn, S., Wehr, N., Gille, P., 2021. Investigating magma ocean solidification on earth through laser-heated diamond anvil cell experiments. *Geophys. Res. Lett.* 48 e2021GL092446.
- Nakagawa, T., Tackley, P.J., 2008. Lateral variations in CMB heat flux and deep mantle seismic velocity caused by a thermal-chemical-phase boundary layer in 3D spherical convection. *Earth Planet. Sci. Lett.* 271, 348–358.
- Nomura, R., Hirose, K., Uesugi, K., Ohishi, Y., Tsuchiyama, A., Miyake, A., Ueno, Y., 2014. Low core-mantle boundary temperature inferred from the solidus of pyrolyte. *Science* 343, 522–525.
- Nomura, R., Zhou, Y., Irfune, T., 2017. Melting phase relations in the MgSiO<sub>3</sub> -CaSiO<sub>3</sub> system at 24 GPa. *Prog. Earth Planet. Sci.* 4, 34.
- O'Neil, H., Canil, D., Rubie, D.C., 1998. Oxide-metal equilibria to 2500°C and 25 GPa: implications for core formation and the light component in the Earth's core. *J. Geophys. Res.* 13, 12239–12260.
- Ono, S., Ohishi, Y., Isshiki, M., Watanuki, T., 2005. In situ X-ray observations of phase assemblages in peridotite and basalt compositions at lower mantle conditions: implications for density of subducted oceanic plate. *JGR: Solid Earth* 110, B02208.
- Pradhan, G.K., Fiquet, G., Siebert, J., Auzende, A.-L., Morard, G., Antonangeli, D., Garbarino, G., 2015. Melting of MORB at core-mantle boundary. *Earth Planet. Sci. Lett.* 431, 247–255.
- Prescher, C., Prakapenka, V.B., 2015. DIOPTAS: a program for reduction of two-dimensional X-ray diffraction data and data exploration. *High Pressure Res.* 35, 223–230.
- Ricard, Y., Richards, M.A., Lithgow-Bertelloni, C., Lestunff, Y., 1993. A geodynamic model of mantle mass heterogeneities. *J. Geophys. Res.* 98, 21895–21909.

- Ricard, Y., Bercovici, D., Schubert, G., 2001. A two-phase model for compaction and damage 2. Applications to compaction, deformation, and the role of interfacial surface tension. *J. Geophys. Res.* 106, 8907–8924.
- Ricard, Y., Labrosse, S., Terasaki, H., Bercovici, D., 2021. Thermocapillary effects in two-phase medium and applications to metal-silicate separation. *Phys. Earth Planet. Inter.* 311, 106640.
- Ricoulleau, A., et al., 2011. Oxygen and silicon contents of Earth's core from high pressure metal-silicate partitioning experiments. *Earth Planet. Sci. Lett.* 310, 409–421.
- Ricoulleau, A., Fei, Y.W., Corgne, A., Siebert, J., Badro, J., 2011. Constraints on oxygen and silicon contents of Earth's core from metal-silicate partitioning experiments at high pressure and temperature. *Earth Planet. Sci. Lett.* 310, 409–421.
- Seto, Y., Nishio-Hamane, D., Nagai, T., Sata, N., 2010. Development of a software suite on X-ray diffraction experiments. *Rev. High Pressure Sci. Technol.* 20 (3), 269–276.
- Shen, G., Lazor, P., 1995. Measurement of melting temperatures of some minerals under lower mantle pressures. *J. Geophys. Res.* 100 (B9), 17699–17713.
- Siebert, J., Corgne, A., Ryerson, F.J., 2011. Systematics of metal-silicate partitioning for many siderophile elements applied to Earth's core formation. *Geochim. Cosmochim. Acta* 75 (6), 1451–1489.
- Siebert, J., Badro, J., Antonangeli, D., Ryerson, F.J., 2012. Metal-silicate partitioning of Ni and Co in a deep magma ocean. *Earth Planet. Sci. Lett.* 321–322, 189–197.
- Sinmyo, R., Hirose, K., 2010. The Soret diffusion in laser-heated diamond-anvil cell. *Phys. Earth Planet. Inter.* 180 (3–4), 172–178.
- Tackley, P.J., Stevenson, D.J., Glatzmaier, G.A., Schubert, G., 1993. Effects of an endothermic phase transition at 670 km depth in a spherical model of convection in the Earth's mantle. *Nature* 361, 699–704.
- Tateno, S., Hirose, K., Ohishi, Y., 2014. Melting experiments on peridotite to lowermost mantle conditions. *J. Geophys. Res. Solid Earth* 119, 4684–4694.
- Tateno, S., Hirose, K., Sakata, S., Yonemitsu, K., Ozawa, H., Hirata, T., 2018. Melting phase relations and element partitioning in MORB to lowermost mantle conditions. *J. Geophys. Res. Solid Earth* 123 (7), 5515–5531.
- Terasaki, H., Urakawa, S., Rubie, D.C., Funakoshi, K.-I., Sakamaki, T., Shibasaki, Y., Ozawa, S., Ohtani, E., 2012. Interfacial tension of Fe-Si liquid at high pressure: implications for liquid Fe-alloy droplet size in magma oceans. *Phys. Earth Planet. Inter.* 202, 1–6.
- Torsvik, T.H., Smethurst, M.A., Burke, K., Steinberger, B., 2006. Large igneous provinces generated from the margins of the large low velocity provinces in the deep mantle. *Geophys. J. Int.* 167, 1447–1460.
- Torsvik, T.H., Burke, K., Steinberger, B., Webb, S.J., Ashwal, L.D., 2010. Diamonds sampled by plumes from the core-mantle boundary. *Nature* 466, 352–355.
- Torsvik, T.H., Steinberger, B., Ashwal, L.D., Doubrovine, P.V., Trønnes, R.G., 2016. Earth evolution and dynamics – a tribute to Kevin Bruce. *Can. J. Earth Sci.* 53, 1073–1087.
- Trønnes, R.G., Baron, M.A., Eigenmann, K.R., Guren, M.G., Løken, A., Mohn, C.E., 2018. Early melting and differentiation, earth and terrestrial planets. *Tectonophysics* 760, 1650–1698.
- van der Hilst, R.D., Widjiantoro, S., Engdahl, E.R., 1997. Evidence for deep mantle circulation from global tomography. *Nature* 386, 578–584.
- van der Meer, D.G., van der Hinsbergen, D.J.J., Spakman, W., 2018. Atlas of the underworld: slab remnants in the mantle, their sinking history, and a new outlook on lower mantle viscosity. *Tectonophysics* 723, 309–448.
- Veksler, I.V., Dorfman, A.M., Borisov, A.A., Wirth, R., Dingwell, D.B., 2007. Liquid immiscibility and the evolution of basaltic magma. *J. Petrol.* 48 (11), 2187–2210.
- Vincenzi, E.P., Green, T.H., Sie, S.H., 1995. Immiscible silicate liquids at high pressure: the influence of melt structure on elemental partitioning. *Nucl. Inst. Methods Phys. Res. B* 104 (1995), 470–475.
- Wade, J., Wood, B.J., 2012. Metal-silicate partitioning experiments in the diamond anvil cell: A comment on potential analytical errors. *Phys. Earth Planet. Inter.* 192–193, 54–58.
- Walter, M.J., Thomson, A.R., Wang, W., Lord, O.T., Ross, J., McMahon, S.C., Baron, M.A., Melekhova, E., Kleppe, A.K., Kohn, S.C., 2015. The stability of hydrous silicates in Earth's lower mantle: experimental constraints from the systems  $MgO-SiO_2-H_2O$  and  $MgO-Al_2O_3-SiO_2-H_2O$ . *Chem. Geol.* 418, 16–29.
- Young, N., Goldstein, J., Block, M., 1959. The motion of bubbles in a vertical temperature gradient. *J. Fluid Mech.* 6 (3), 350–356.